Featured in Physics

Quantitative characterization of run-and-tumble statistics in bulk bacterial suspensions

Yongfeng Zhao [1,2,3,4,*,†] Christina Kurzthaler [5,6,7,8,*,‡] Nan Zhou [9] Jana Schwarz-Linek [10] Clemence Devailly [10]
Jochen Arlt [10] Jian-Dong Huang [3,11] Wilson C. K. Poon [10] Thomas Franosch [8] Vincent A. Martinez [10]
and Julien Tailleur [4,§]

[1]*Center for Soft Condensed Matter Physics and Interdisciplinary Research & School of Physical Science and Technology,
Soochow University, Suzhou 215006, China*
[2]*School of Physics and Astronomy and Institute of Natural Sciences, Shanghai Jiao Tong University, Shanghai 200240, China*
[3]*School of Biomedical Sciences, Li Ka Shing Faculty of Medicine, University of Hong Kong,
Pok Fu Lam, Hong Kong, People's Republic of China*
[4]*Université de Paris, MSC, UMR 7057 CNRS, 75205 Paris, France*
[5]*Max Planck Institute for the Physics of Complex Systems, 01187 Dresden, Germany*
[6]*Center for Systems Biology Dresden, 01307 Dresden, Germany*
[7]*Department of Mechanical and Aerospace Engineering, Princeton University, Princeton, New Jersey 08544, USA*
[8]*Institut für Theoretische Physik, Universität Innsbruck, Technikerstraße 21A, A-6020 Innsbruck, Austria*
[9]*ZJU-Hangzhou Global Scientific and Technological Innovation Center, Zhejiang University, Hangzhou 311200, China*
[10]*School of Physics and Astronomy, University of Edinburgh, James Clerk Maxwell Building, Peter Guthrie Tait Road, Edinburgh EH9 3FD,
United Kingdom*
[11]*CAS Key Laboratory of Quantitative Engineering Biology, Shenzhen Institute of Synthetic Biology, Shenzhen Institutes of Advanced
Technology, Chinese Academy of Sciences, Shenzhen 518055, China*

We introduce a numerical method to extract the parameters of run-and-tumble dynamics from experimental measurements of the intermediate scattering function. We show that proceeding in Laplace space is unpractical and employ instead renewal processes to work directly in real time. We first validate our approach against data produced using agent-based simulations. This allows us to identify the length and time scales required for an accurate measurement of the motility parameters, including tumbling frequency and swim speed. We compare different models for the run-and-tumble dynamics by accounting for speed variability at the single-cell and population level, respectively. Finally, we apply our approach to experimental data on wild-type *Escherichia coli* obtained using differential dynamic microscopy.

I. INTRODUCTION

A hallmark of many living microorganisms is their ability to self-propel in liquid environments [1–3]. To optimize their survival strategies, such as foraging [4] and escaping from harm [5], many microorganisms employ reorientation mechanisms in addition to their directed swimming motion. During reorientation events, cells change their swimming direction through microorganism-specific processes. Examples range from the "run-reverse(-flick)" patterns employed by several marine bacteria [6,7] and archaea [8], to the "run-reverse-wrap" modes of *Pseudonmas putida* [9], to the random change of the swimming direction of the algae *Chlamydomonas reinhardtii* due to the buckling of one of their cilia [10]. The most widely studied microorganism is probably the bacterium *Escherichia coli*, which performs paradigmatic "run-and-tumble" (RT) motion [11–14].

The motion of *E. coli* in bulk is characterized by two alternating phases: a running and a tumbling phase. In the running phase, bacteria swim persistently with an almost constant speed. "Running" bacteria stochastically enter a tumbling phase due to the random unbundling of one or several of their flagella. During a tumble, bacteria undergo rotational diffusion before they resume swimming in a new direction [15]. In a homogeneous environment, this RT motion resembles a random walk at large length and time scales [11,12,16,17]. Such an RT motility pattern becomes drastically altered in the presence of surfaces, which can induce circular motion via hydrodynamic couplings [18,19] and trap the microorganisms until a tumbling event allows them to escape [20]. Thus, the quantitative characterization of the RT dynamics requires a 3D bulk study, far from perturbing boundaries.

Due to the significant biological importance of the tumbling statistics for, e.g., bacterial chemotaxis, the underlying genetics and biochemistry have been studied extensively [5]. The dynamics of individual flagella have been measured *in*

---

*These authors contributed equally to this work.

†yfzhao2021@suda.edu.cn

‡ckurzthaler@pks.mpg.de

§julien.tailleur@univ-paris-diderot.fr

vitro using single-motor experiments [21,22]. A quantitative characterization in three dimensions and at the population level, however, has remained a challenge. Tracking single-cell trajectories in three dimensions requires a low cell concentration and is limited to short trajectories. The statistical accuracy is therefore often insufficient to reliably extract the tumbling statistics.

Differential dynamic microscopy (DDM) is a possible alternative for studying the motion of microswimmers [23]. It measures the intermediate scattering function (ISF), $f(\mathbf{k}, \tau)$, i.e., the probability density at lag time τ of particle displacements $\Delta \mathbf{r}$ in Fourier space:

$$f(\mathbf{k}, \tau) = \langle e^{-i\mathbf{k} \cdot \Delta \mathbf{r}(\tau)} \rangle. \quad (1)$$

The ISF is usually computed by averaging over a large number of agents ($\gtrsim 10^4$ for *E. coli* in Ref. [24]), which provides reasonable statistics at the population level. Fitting the experimentally measured ISF to a theoretical model can then give access to the motility parameters of the microorganisms. While recent work on catalytic Janus colloids has resolved the transition from persistent motion to a randomization of the swimming direction due to rotational diffusion in two dimensions [25], the swimming properties of microorgansims in bulk have been measured only up to length scales of a persistence length [24,26–28].

Although quantifying the tumbling statistics at larger length scales using DDM may appear to be merely an extension of previous work [24], it has remained out of reach so far. Theoretically, the difficulty lies in the nonexistence of an analytical form of the ISF in three dimensions in the time domain. Although its Laplace transform is known [29,30], fitting the ISF in Laplace space to the Laplace transform of the discrete data is often problematic, due to the significant integration error introduced by the finite data sequence. Thus, one has to calculate the ISF in the time domain.

Here we propose two strategies for calculating the ISF of RT particles in real time, based on a renewal theory: (1) We solve the renewal equations in Fourier space numerically, which immediately provides the ISF and (2) we compute the numerical inverse of the ISF in Laplace space, which is known analytically. (We note that fitting the data in Laplace space always proves unpractical.) Both methods can, in principle, be used equivalently and be applied for various scenarios. However, in practice, they are suitable for different situations: For particles with an intrinsic variability of swim speed and with arbitrary running and tumbling time distributions, option 1 is the only route. For particles with a speed variability at the population level, the direct inverse Laplace transform (option 2) is easier to compute, but this strategy is restricted to exponential running and tumbling time distributions.

The paper is organized as follows: In Sec. II we introduce the renewal theory and compare the models with speed variability at the single-cell and population level. In Sec. III we present a robust protocol for the parameter estimation, which we validate using simulated data. In Sec. IV we analyze the data of wild-type *E. coli* using the model with speed variability at the population level and compare it to the results from Ref. [31], where an intrinsic variability of swimming speed was assumed. Finally we summarize our results in Sec. V.
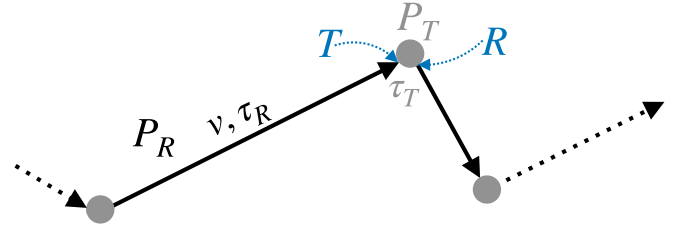
FIG. 1. Schematic of the run-and-tumble motion of a particle with mean run and tumbling times, τ_R and τ_T, respectively. The particle moves at velocity v during the run phase. P_R and P_T are the probabilities of the swimmer to be in a run or tumbling phase. T and R denote the probabilities to start tumbling or running, respectively.

II. RENEWAL THEORY

We consider a model of RT bacterium alternating between persistent runs in quasistraight lines and finite-duration tumbles during which the cells fully randomize their directions [11–14,29] (see Fig. 1). The probability to find a bacterium displaced by a distance $\mathbf{r}$ after a lag time τ is $P(\mathbf{r}, \tau) = P_R(\mathbf{r}, \tau) + P_T(\mathbf{r}, \tau)$, where $P_R(\mathbf{r}, \tau)$ and $P_T(\mathbf{r}, \tau)$ correspond to the probability to be at position $\mathbf{r}$ after a lag time τ and to be in a running or tumbling phase, respectively. The ISF of noninteracting bacteria is then obtained via a Fourier transform: $f_{RT}(\mathbf{k}, \tau) = \int d^3r \exp(-i\mathbf{k} \cdot \mathbf{r}) P(\mathbf{r}, \tau)$. We denote by $\varphi_R(\tau)$ and $\varphi_T(\tau)$ the distributions of the durations of the RT phases, respectively. To allow for generic distributions, which need not correspond to Markovian processes, we also introduce the probabilities that a bacterium *starts* running or tumbling at displacement $\mathbf{r}$ and lag time τ, which we denote by $R(\mathbf{r}, \tau)$ and $T(\mathbf{r}, \tau)$, respectively. Finally, the propagators $\mathbb{P}_R(\mathbf{r}, \tau)$ and $\mathbb{P}_T(\mathbf{r}, \tau)$ measure the probability that a bacterium travels a distance $\mathbf{r}$ during a time τ in a running or a tumbling phase, respectively.

To compute the ISF, we describe the RT dynamics as a renewal process [32–34] for which $P_R(\mathbf{r}, \tau)$ satisfies

$$P_R = P_R^0 + \int_0^\tau dt \int d^3\ell \, R(\mathbf{r} - \boldsymbol{\ell}, \tau - t) \varphi_R^0(t) \mathbb{P}_R(\boldsymbol{\ell}, t), \quad (2)$$

where $\varphi_R^0(t) := \int_t^\infty dt' \, \varphi_R(t')$ is the probability that the run time exceeds t. Let us define the average times spent running or tumbling, $\tau_{R,T} = \int_0^\infty dt \, t \varphi_{R,T}(t)$. The probability that a particle is running at time 0 is then equal to the fraction of time the cell spends running: $p_R = \tau_R / (\tau_R + \tau_T)$. Further, we denote the probability that the bacterium arrives in $\mathbf{r}$ at time τ without having tumbled in $[0, \tau]$ by $P_R^0(\mathbf{r}, \tau)$. It is given by the probability $K(\tau)$ that the cell is in a running state at $t = 0$ and remains in this state for a time $t > \tau$, multiplied by the propagator $\mathbb{P}_R(\mathbf{r}, \tau)$ and the probability p_R. Because the dynamics is not necessarily Markovian, the computation of $K(\tau)$ is not straightforward. It is given by the joint probability that $t = 0$ falls in a run phase of duration t larger than τ, which has a probability density $t\varphi_R(t)/\tau_R$, and that the remaining time before the next tumble is larger than τ, which has a probability $(t - \tau)/t$ when $t > \tau$ (and vanishes otherwise). This leads to [35]

$$K(\tau) = \int_\tau^\infty dt \, \varphi_R(t)(t - \tau)/\tau_R. \quad (3)$$

All in all, we find

$$P_R^0(\mathbf{r}, \tau) := p_R \mathbb{P}_R(\mathbf{r}, \tau) \int_\tau^\infty \mathrm{d}t \, \varphi_R(t)(t - \tau)/\tau_R. \quad (4)$$

Intuitively, Eq. (2) states that the probability to be at $\mathbf{r}$ at time τ is the sum of the probabilities of arriving in $\mathbf{r}$ without tumbling in $[0, \tau]$, P_R^0, and with at least one tumble. In the second case, the last tumble takes place at arbitrary displacements $\mathbf{r} - \boldsymbol{\ell}$ and lag times $\tau - t$, which should be summed over. Similarly, the probability that the bacterium starts a new run at displacement $\mathbf{r}$ and lag time τ, $R(\mathbf{r}, \tau)$, takes into account the possibility that this is the first run or that a run has already finished at $\tau - t$ and $\mathbf{r} - \boldsymbol{\ell}$:

$$R = R^1 + \int_0^\tau \mathrm{d}t \int \mathrm{d}^3\ell \, T(\mathbf{r} - \boldsymbol{\ell}, \tau - t)\varphi_T(t)\mathbb{P}_T(\boldsymbol{\ell}, t). \quad (5)$$

Here $R^1(\mathbf{r}, \tau) := (1 - p_R)\mathbb{P}_T(\mathbf{r}, \tau) \int_\tau^\infty \mathrm{d}t \, \varphi_T(t)/\tau_T$ is the probability of starting the first run in $\mathbf{r}$ at time τ [35]. By swapping R and T everywhere in Eqs. (2)–(5) we obtain two other (formally identical) renewal equations for the probabilities $P_T(\mathbf{r}, \tau)$ and $T(\mathbf{r}, \tau)$:

$$P_T = P_T^0 + \int_0^\tau \mathrm{d}t \int \mathrm{d}^3\ell \, T(\mathbf{r} - \boldsymbol{\ell}, \tau - t)\varphi_T^0(t)\mathbb{P}_T(\boldsymbol{\ell}, t), \quad (6)$$

$$T = T^1 + \int_0^\tau \mathrm{d}t \int \mathrm{d}^3\ell \, R(\mathbf{r} - \boldsymbol{\ell}, \tau - t)\varphi_R(t)\mathbb{P}_R(\boldsymbol{\ell}, t). \quad (7)$$

An RT dynamical model is then entirely determined by the propagators $\mathbb{P}_{R,T}$ and by the choice of the reorientation process specified by the distribution $\varphi_{R,T}$ from which $P_{R,T}^0$, R^1, and T^1 follow. Since the renewal equations couple all positions and times, they are hard to solve in $\mathbf{r}$-space. Exploiting the convolution theorem, a Fourier transform yields a set of equations that are decoupled in Fourier space. Due to the isotropy of the system, they depend only on the wave number $k = |\mathbf{k}|$ and can be solved for each k separately. Equations (2)–(7) lead to

$$P_R(k, \tau) = P_R^0(k, \tau) + \int_0^\tau \mathrm{d}t \, R(k, \tau - t)\varphi_R^0(t)\mathbb{P}_R(k, t), \quad (8)$$

$$R(k, \tau) = R^1(k, \tau) + \int_0^\tau \mathrm{d}t \, T(k, \tau - t)\varphi_T(t)\mathbb{P}_T(k, t), \quad (9)$$

$$P_T(k, \tau) = P_T^0(k, \tau) + \int_0^\tau \mathrm{d}t \, T(k, \tau - t)\varphi_T^0(t)\mathbb{P}_T(k, t), \quad (10)$$

$$T(k, \tau) = T^1(k, \tau) + \int_0^\tau \mathrm{d}t \, R(k, \tau - t)\varphi_R(t)\mathbb{P}_R(k, t). \quad (11)$$

Once a given RT dynamical model is chosen, Eqs. (8)–(11) permit numerical evaluation of the ISF for RT particles, $f_{RT}(k, \tau) = P_R(k, \tau) + P_T(k, \tau)$.

Inspection of Eqs. (8)–(11) suggests that analytical progress can be made in Laplace space, following [29]. In particular, a Laplace transform of Eqs. (8)–(11) yields the propagators, P_R and P_T, for arbitrary RT distributions, φ_R and φ_T, and probabilities, $\mathbb{P}_R$ and $\mathbb{P}_T$:

$$P_R(k, s) = P_R^0(k, s) + \mathcal{L}\big[\varphi_R^0(\tau)\mathbb{P}_R(k, \tau)\big](s)\frac{R^1(k, s) + T^1(k, s)\mathcal{L}[\varphi_T(\tau)\mathbb{P}_T(k, \tau)](s)}{1 - \mathcal{L}[\varphi_R(\tau)\mathbb{P}_R(k, \tau)](s)\mathcal{L}[\varphi_T(\tau)\mathbb{P}_T(k, \tau)](s)}, \quad (12)$$

$$P_T(k, s) = P_T^0(k, s) + \mathcal{L}\big[\varphi_T^0(\tau)\mathbb{P}_T(k, \tau)\big](s)\frac{T^1(k, s) + R^1(k, s)\mathcal{L}[\varphi_R(\tau)\mathbb{P}_R(k, \tau)](s)}{1 - \mathcal{L}[\varphi_T(\tau)\mathbb{P}_T(k, \tau)](s)\mathcal{L}[\varphi_R(\tau)\mathbb{P}_R(k, \tau)](s)}, \quad (13)$$

where $\mathcal{L}[f(\tau)](s) := \int_0^\infty \mathrm{d}\tau \exp(-s\tau)f(\tau)$ denotes the Laplace transform of a function $f(\tau)$.

A. Intrinsic speed variability

So far we have introduced the general framework of a renewal process switching between the running and tumbling phases. Let us now specify the time distributions $\varphi_{R,T}$ and the propagators $\mathbb{P}_{R,T}$ for RT particles. We first consider the case in which a bacterium changes its swim speed after each tumble, which we refer to as *intrinsic speed variability*. This accounts for the fluctuations of the propulsion speed over time that have recently been reported experimentally [36]. Alternatively, the distribution of swimming speed can be accounted for at the population level, leading to a different model discussed in Sec. II B.

For simplicity, we here consider exponential distributions for the run and tumbling times with $\varphi_{R,T}(t) = \exp(-t/\tau_{R,T})/\tau_{R,T}$, where τ_R and τ_T denote the mean run and tumbling durations, respectively. We note, however, that our formalism allows discussing more general distributions as well. We now discuss the propagators $\mathbb{P}_R$ and $\mathbb{P}_T$.

Assuming that tumbling particles diffuse with diffusivity D, the corresponding propagator is given by

$$\mathbb{P}_T(k, \tau) = \exp(-Dk^2\tau). \quad (14)$$

For a swimming particle with speed v and thermal diffusion constant D, the propagator instead reads $\exp(-Dk^2\tau)\sin(vk\tau)/(vk\tau)$. Assuming that, after each tumble, the particle samples a new swimming speed from a distribution $p(v)$, the propagator of the swimming particles is

$$\mathbb{P}_R(k, \tau) = \int_0^\infty p(v)\exp(-Dk^2\tau)\frac{\sin(vk\tau)}{vk\tau} \, \mathrm{d}v. \quad (15)$$

We use the Schulz distribution, which is characterized by a mean velocity $\bar{v}$ and standard deviation σ_v [26],

$$p(v) = \frac{v^Z}{\Gamma(Z + 1)}\left(\frac{Z + 1}{\bar{v}}\right)^{Z+1} e^{-(Z+1)v/\bar{v}}, \quad (16)$$

with $Z = \bar{v}^2/\sigma_v^2 - 1$. Then $\mathbb{P}_R(k, \tau)$ can be computed analytically as

$$\mathbb{P}_R(k, \tau) = e^{-Dk^2\tau}\left(\frac{Z + 1}{Zk\bar{v}\tau}\right)\frac{\sin(Z\arctan\xi)}{(1 + \xi^2)^{Z/2}}, \quad (17)$$

with $\xi = k\bar{v}\tau/(Z + 1)$.
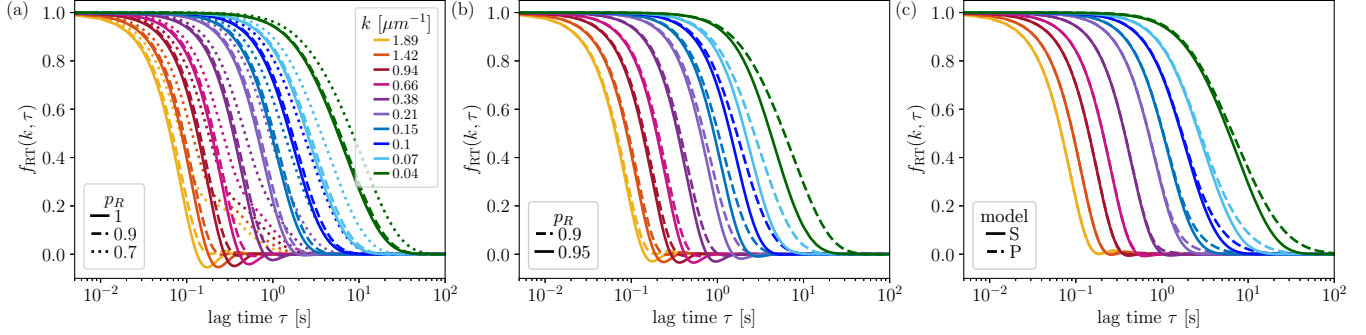
FIG. 2. ISFs, $f_{RT}(k, \tau)$, for our RT model. (a), (b) Intrinsic speed variability model for different fractions of run times $p_R = \tau_R/(\tau_R + \tau_T)$. In (a) we vary the tumbling time with parameter values $\tau_R = 1$ s and $\tau_T = 0, 0.1, 0.5$ s, and in (b) we vary the run time, $\tau_T = 0.1$ s and $\tau_R = 2, 1$ s. The other motility parameters are $\bar{v} = 15 \, \mu\mathrm{m \, s^{-1}}$, $\sigma_v = 4.5 \, \mu\mathrm{m \, s^{-1}}$, and $D = 0.3 \, \mu\mathrm{m^2 \, s^{-1}}$. (c) Comparison of the ISF for the model with speed fluctuations at the single cell (S; solid line) and population (P; dashed line) level using identical parameters ($\tau_R = 1$ s, $\tau_T = 0.1$ s, $\bar{v} = 15 \, \mu\mathrm{m \, s^{-1}}$, $\sigma_v = 4.5 \, \mu\mathrm{m \, s^{-1}}$, and $D = 0.3 \, \mu\mathrm{m^2 \, s^{-1}}$).

Using Eqs. (14) and (17) as input, we can solve the integral equations (8)–(11) numerically by time stepping τ for each wave number separately. This then leads to the intermediate scattering function (ISF) for the run-and-tumble particle, $f_{RT}(k, t) = P_R(k, \tau) + P_T(k, \tau)$.

We note that the Laplace transform obtained from Eqs. (12) and (13) involves hypergeometric functions, which makes its numerical inversion cumbersome and inefficient using Weeks' method [37,38].

B. Speed variability at the population level

Alternatively, one could consider a model, where the speed v of a given bacterium is constant, but where v is distributed over the bacterial population. As we show below, this leads to a simpler expression in Laplace space but does not account for temporal fluctuations of v at the single-bacterium level.

Again, the speed distribution $p(v)$ of the population is chosen to be a Schultz distribution. In particular, within the renewal framework we replace the propagator for the run phase by $\mathbb{P}_R(k, \tau) = \exp(-Dk^2 \tau) \sin(vk\tau)/(vk\tau)$. Then the ISF is obtained by postaveraging the ISF of a single cell over the speed distribution, $f_{RT}(k, \tau) = \int dv \, p(v)[P_R(k, \tau) + P_T(k, \tau)]$. The two models are not equivalent due to the nonlinearity of Eqs. (12) and (13) with respect to the propagators $\mathbb{P}_{R,T}$.

For this model, the numerical evaluation of the ISF, $f_{RT}(k, \tau)$, is expensive within the renewal framework due to the final integration over $p(v)$. Fortunately, the Laplace transform, $f_{RT}(k, s)$, is simpler than in the intrinsic-speed-variability model. Substituting the propagators, $\mathbb{P}_R(k, \tau)$ and $\mathbb{P}_T(k, \tau) = \exp(-Dk^2 \tau)$, and the exponential RT distributions, φ_R and φ_T, into Eqs. (12) and (13), the ISF in Laplace space for a population of noninteracting RT particles with speed distribution reads

$$f_{RT}(k, s) = \int_0^\infty dv \, p(v) \frac{kv\tau_T^2\tau_R + \tau_R[\tau_R + 2\tau_T + \tau_T\tau_R(Dk^2 + s)] \arctan[kv\tau_R/(Dk^2\tau_R + 1 + s\tau_R)]}{(\tau_R + \tau_T)\{kv\tau_R(1 + \tau_T Dk^2 + \tau_T s) - \arctan[kv\tau_R/(Dk^2\tau_R + 1 + s\tau_R)]\}}. \tag{18}$$

Note that for exponentially distributed RT times, the ISF in Laplace space could also be obtained by generalizing the method introduced in Ref. [30] for finite-duration tumbles. The time-domain ISF $f_{RT}(k, \tau)$ can be computed from Eq. (18) using the standard Weeks' method [37,38]. Before discussing our fitting procedure and its validation using simulated data in Sec. III, we first show below how the ISFs depend on the ingredients of the RT dynamics and the source of speed fluctuations.

C. Intermediate scattering functions

Figures 2(a) and 2(b) show the ISFs for the RT model with intrinsic speed variability evaluated for motility parameters measured for *E. coli* (see figure caption). The calculated ISFs $f_{RT}(k, \tau)$ [Fig. 2(a)] show a clear evolution at short times and small length scales $\ell = 2\pi/k$ as one varies the RT durations close to their estimated biological values of $\tau_T \simeq 0.1$ s and

$\tau_R \simeq 1$ s [11]. For instantaneous tumbles, $\tau_T = 0$ ($p_R = 1$), the ISFs display oscillations for large k, which are smeared and disappear at times $\tau \gtrsim \tau_R$ and at small wave numbers $k \lesssim 0.38 \, \mu\mathrm{m^{-1}}$ corresponding to a length scale $\ell \approx 16.5 \, \mu\mathrm{m}$, comparable with the persistence length $\ell_p = \langle v \rangle \tau_R = 15 \, \mu\mathrm{m}$ beyond which the motion becomes randomized by tumbles. As the tumble duration increases (p_R decreases), oscillations fade out until a hump develops ($\tau_T = 0.5$ s, $p_R \approx 0.7$) due to the diffusive motion of tumbling bacteria at small ℓ.

Figure 2(b) shows the ISFs for a fixed tumble duration of $\tau_T = 0.1$ s and varying run time $\tau_R = 2, 1$ s. As the run time increases, we observe stronger oscillations at short times $\tau \lesssim \tau_R$ and large wave numbers k and a more rapidly decreasing ISF at small wave numbers, which indicates that the regime of effective diffusion emerges at larger length and time scales. This pattern of behavior suggests that, in principle, experimentally measured ISFs should contain enough information
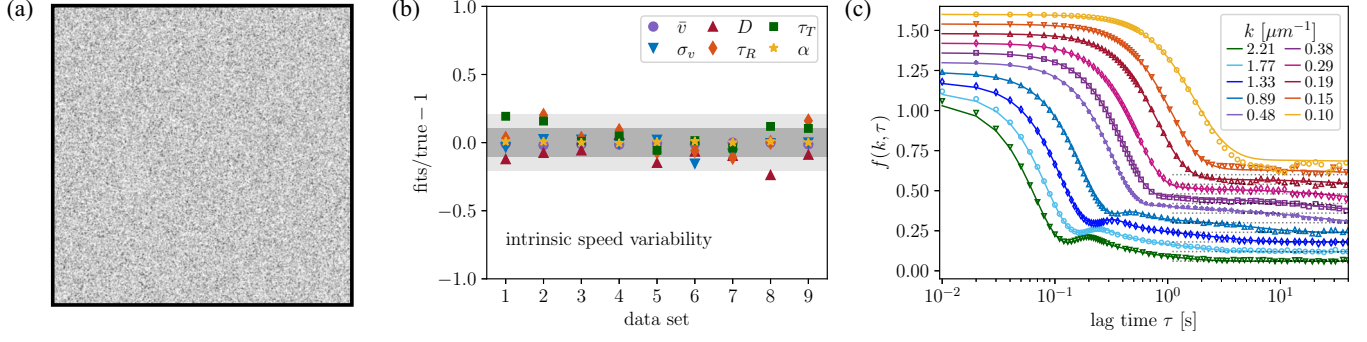
FIG. 3. (a) Snapshot of a RT simulation with the low magnification (see Appendix B). (b), (c) Validation of theoretical predictions with simulations for nine parameter sets with $\bar{v} = 17 \ \mu m \, s^{-1}$, $\sigma_v = 4.3 \ \mu m \, s^{-1}$, $D = 0.3 \ \mu m^2 \, s^{-1}$, $\alpha = 0.9$, varying the mean run and tumbling times, $\tau_R \in [0.5, 1.5]$ s and $\tau_T \in [0.1, 0.5]$ s. (b) Parameter estimates obtained by fitting theoretical predictions of the ISF to agent-based simulations. The estimates are compared with the true parameters for the nine data sets. They were extracted from a global fit including wave numbers $k \in [0.15, 2.21] \ \mu m^{-1}$. Dark gray regions correspond to fitted parameters within $\pm 10\%$ of the true values (light gray corresponds to $\pm 20\%$). (c) ISF, $f(k, \tau)$, for $\tau_R = 1.25$ s, $\tau_T = 0.2$ s (data set 8) and different wave numbers k. Theoretical predictions and simulations correspond to lines and symbols, respectively. The ISFs are shifted w.r.t. the y axis and the gray dotted lines indicate $y = 0$.

to characterize all features of the RT dynamics of *E. coli*, including the tumbling statistics.

Finally, we compare the ISFs for both models; see Fig. 2(c). In particular, we observe that at short times and length scales the ISFs of both models are almost indistinguishable, and hence the fingerprint of the speed variability on the ISFs is subtle. The effect, however, becomes visible in our theory at large length scales, corresponding to $k \gtrsim 0.38 \ \mu m^{-1}$. Whether this small difference of the ISFs will be measurable and identifiable from experiments will be discussed later.

III. NUMERICAL PROTOCOL AND VALIDATION ON SIMULATED DATA

We next present the numerical protocol that allows us to estimate the motility parameters of bacteria, such as their mean RT times and swimming speed, from measured ISFs. For the sake of completeness, we first recall below how ISFs are measured experimentally using differential dynamic microscopy (DDM).

A. Differential dynamic microscopy

DDM is a high-throughput method that provides quantitative information on 3D swimming microorganisms through their ISF; see Refs. [23,26] for details. Briefly, the differential image correlation function (DICF), $g(\mathbf{k}, \tau)$, i.e., the power spectrum of the difference between pairs of images separated by time τ, is obtained via $g(\mathbf{k}, \tau) = \langle |I(\mathbf{k}, t + \tau) - I(\mathbf{k}, t)|^2 \rangle_t$, where $I(\mathbf{k}, t)$ is the Fourier transform of the image $I(\mathbf{r}, t)$ and $\langle \cdot \rangle_t$ denotes an average over time t. Under suitable imaging conditions and for isotropic motion, the DICF is related to the ISF [24,26,39], $f(k, \tau)$, via

$$g(k, \tau) = \langle g(\mathbf{k}, \tau) \rangle_{\hat{\mathbf{k}}} = A(k)[1 - f(k, \tau)] + B(k) \quad (19)$$

with $\langle \cdot \rangle_{\hat{\mathbf{k}}}$ denoting average over the directions $\hat{\mathbf{k}} \equiv \mathbf{k}/|\mathbf{k}|$, and $A(k)$ and $B(k)$ the signal amplitude and instrumental noise, respectively. These coefficients are obtained from the plateau

of $g(k, \tau)$ at long and short times, where the ISF approaches $f(k, \tau \to \infty) \to 0$ and $f(k, \tau \to 0) \to 1$, respectively.

B. Fitting procedure

To reliably extract quantitative information from the measured ISFs using our renewal theory, we implement a fitting procedure based on the minimization of the squared errors using a Nelder-Mead optimization algorithm [40]. We apply a multistart fitting analysis, where several fits are obtained for various initial values and the parameter set yielding the smallest error is chosen. In most fitting procedures several initial values provided the same result, which strengthens the reliability of our procedure.

We performed a global fit including data for several wave numbers simultaneously. Using one data set, we tested several wave-number ranges and found the most adequate should include length scales of the order of the cell body, up to length scales resolving the randomization of the swimming direction, i.e., $k\ell_p \lesssim 2\pi$. The parameter estimation method has been validated with simulations (see Sec. III C).

C. Validation of the fitting procedure

Before tackling the experimental data, we have validated our parameter estimation method with computer simulations (see Appendix B). To do so, we consider exponentially distributed RT times with different τ_R and τ_T, which are close to those reported previously [11]. In particular, we set $\tau_R \in [0.5, 1.5]$ s and $\tau_T \in [0.1, 0.5]$ s corresponding to $p_R = \tau_R/(\tau_R + \tau_T) \in [0.67, 0.91]$. We further choose values for the remaining motility parameters, including the mean velocity, $\bar{v}$, its standard deviation, σ_v, the translational diffusivity, D, that are typical for *E. coli* suspensions [24,26]. Following experimental findings [31], we add a fraction $1 - \alpha$ of non-motile cells that undergo Brownian motion with diffusivity D in the simulations. Thus the ISF obtained from simulated data should follow

$$f(k, \tau) = \alpha f_{RT}(k, \tau) + (1 - \alpha) e^{-Dk^2 \tau}. \quad (20)$$
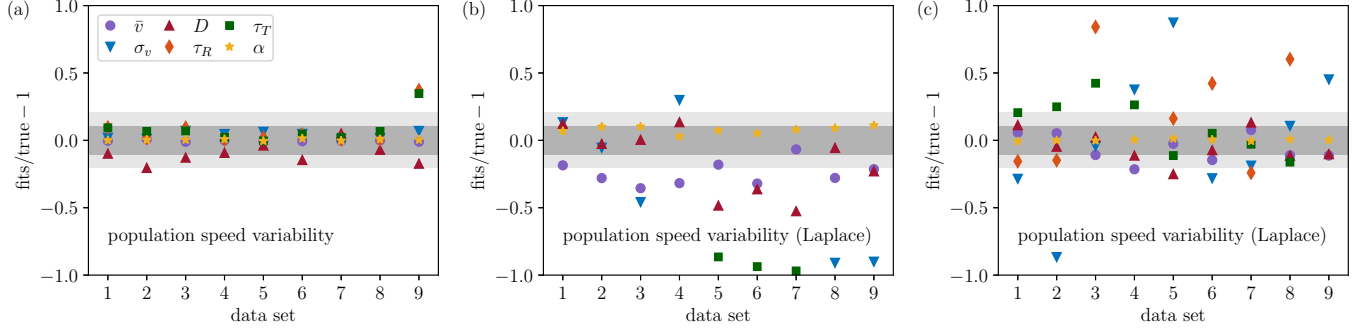
FIG. 4. Parameter estimates obtained by fitting theoretical predictions of the ISF to agent-based simulations with speed variability at the population level. Parameters are the same as in Fig. 3: $\bar{v} = 17\ \mu\mathrm{m\,s^{-1}}$, $\sigma_v = 4.3\ \mu\mathrm{m\,s^{-1}}$, $D = 0.3\ \mu\mathrm{m^2\,s^{-1}}$, $\alpha = 0.9$. The mean run and tumbling times are varied within $\tau_R \in [0.5, 1.5]$ s and $\tau_T \in [0.1, 0.5]$ s. (a) Fitting in lag time τ with numerical inverse Laplace transform of theoretical ISF. (b, c) Fitting in Laplace time s using the numerical Laplace transform of the data, with s ranging from (b) $1/\tau_{\max}$ to $1/\tau_{\min}$ and (c) $10/\tau_{\max}$ to $1/\tau_{\min}$. The estimates are compared with their true values for the nine data sets. Outliers with an error such that $(\mathrm{fits/true}-1) > 1$ are not shown. We used a global fit including wave numbers $k \in [0.15, 2.21]\ \mu\mathrm{m^{-1}}$. Dark gray regions correspond to fitted parameters within $\pm 10\%$ error of the true values (light gray corresponds to $\pm 20\%$).

First, we perform simulations of the intrinsic-speed variability model. We employ a global fitting procedure (as outlined in Sec. III B) and simultaneously include wave numbers $k \in [0.15, 2.21]\ \mu\mathrm{m^{-1}}$. Fitting our renewal theory to the ISF extracted from simulated data of particles with intrinsic speed variability reveals that our fitting protocol reliably reproduces the true parameter values. In particular, most of the fitted parameters lie within $\pm 10\%$ error with respect to the true values [Fig. 3(b)]. Figure 3(c) shows excellent agreement between the simulated ISF with mean run and tumbling times, $\tau_R = 1.25$ s, $\tau_T = 0.2$ s (data set 8), and the theoretical predictions obtained from the fitting procedure.

We also perform simulations of a mixture of particles with different speeds, fixing each particle speed during the simulation. We use the inverse Laplace transform of Eq. (18) to calculate the ISF. Including a fraction α of nonmotile cells, we follow the same global fitting procedure as introduced in Sec. III B to fit the data. We find that the fitted parameters again lie within $\pm 10\%$ error with respect to the true values [Fig. 4(a)].

Note that fitting the expression (18) directly in Fourier-Laplace space over the full range $s \in [1/\tau_{\max}, 1/\tau_{\min}]$ leads to large, systematic errors for most parameters [Fig. 4(b)]. These errors are mainly due to the loss of numerical precision during integration of the discrete data to calculate their Laplace transform. Using a smaller range $s \in [10/\tau_{\max}, 1/\tau_{\min}]$ [Fig. 4(c)] slightly improves the fitting results but does not lead to satisfactory estimates, especially for the tumbling and running durations. We further note that while an optimized s range may lead to a satisfactory fit in Laplace space, it requires *a priori* knowledge of the swimming parameters that makes this procedure unsatisfactory. This is a major issue for the analysis of experimental data, which probably explains why DDM has not been used so far to characterize RT dynamics, despite the explicit expressions for the propagators in Fourier-Laplace space [29,30]. For numerics as well as experimental data, we found that the renewal theory was always a more efficient and reliable avenue.

IV. EXPERIMENTS

We now demonstrate that our numerical protocol can indeed be used to characterize quantitatively experimental data. To do so, we use the data on the wild-type AB1175 *E. coli* strain presented in our joint work [31]. In short, these data were obtained by imaging swimming cells in sealed capillaries on a fully automated inverted bright-field microscope with a sCMOS camera. To characterize the RT dynamics we require access to length scales larger than the cells' persistence length, $\gtrsim \ell_p$, in 3D. Therefore, a large depth of field at low k is needed to ensure that bacteria remain in view over large distances in all directions. To measure the dynamics at all relevant length scales, we consecutively recorded movies at $2\times$ and $10\times$ magnifications to extract the ISF for $k < 0.9\ \mu\mathrm{m^{-1}}$ and $k \geqslant 0.9\ \mu\mathrm{m^{-1}}$, respectively, using standard DDM procedures [24,26]. The low- and high-magnification data were recorded at a frame rate of 0.02 s and 0.01 s over 300 s and 80 s, respectively. We refer to the Supplemental Material of Ref. [31] for more details on the experimental procedure. Fitting the ISFs to our renewal theory using the numerical protocol described here yields RT motility parameters.

We have reported the fitting results from the intrinsic-speed-variability model in Fig. 4 of Ref. [31]. Here we fit the same data to the theoretical predictions of the model that incorporate speed fluctuations at the bacterial population level, using the numerical inverse Laplace transform of Eq. (18). We obtain the following motility parameters: $\alpha = 97 \pm 0.3\%$, $\bar{v} = 16 \pm 0.2\ \mu\mathrm{m\,s^{-1}}$, $\sigma_v = 5.80 \pm 0.29\ \mu\mathrm{m\,s^{-1}}$, $D = 0.25 \pm 0.04\ \mu\mathrm{m^2\,s^{-1}}$, $\tau_R = 3.21 \pm 0.38$ s, $\tau_T = 0.50 \pm 0.05$ s. The corresponding ISFs are shown in Fig. 5 and display nice agreement with the experimental data.

The estimates for the motility parameters are largely consistent with those reported in Ref. [31], although they were obtained from fitting a slightly different model. We note the fraction of running time $\tau_R/(\tau_R + \tau_T) = 0.866$ agrees with the well-cited results from Berg and Brown [11] and the fits in Ref. [31] ($\tau_R/(\tau_R + \tau_T) = 0.863$). This suggests that the origin of the speed variability is indistinguishable under
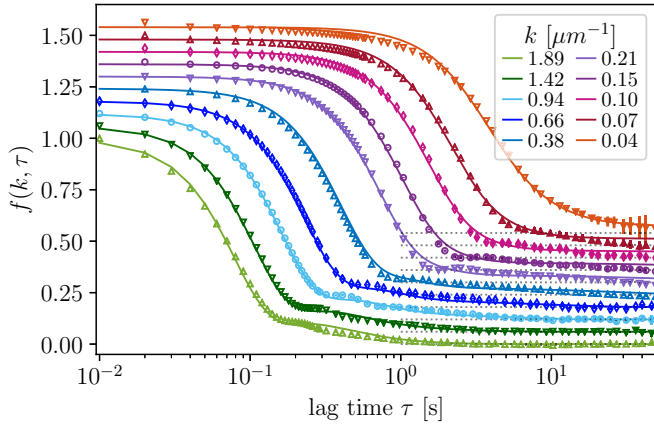
FIG. 5. ISFs for different wave numbers k. Symbols represent experimental results for *E. coli* bacteria (same as in Fig. 3 of Ref. [31]), and lines are the theoretical predictions obtained by considering speed variability at population level. The data are fitted to the numerical inverse of Eq. (18) including wave numbers $k \in [0.04, 1.89] \, \mu\text{m}^{-1}$.

the spatiotemporal scales measured in the experiments. To show this, we used the measured experimental parameters to produce simulation data using both models. We then fitted the intrinsic-speed-variability simulation data with the population-level-speed-variability ISFs, and vice versa. In both cases, the "wrong" models fit the data rather well. A natural question then arises regarding the conditions under which the two models could be distinguished using ISF measured with our experimental setup. As shown in Fig. 6, a wider speed distribution would make the ISF distinguishable at small k. Indeed, the fits lead to a smaller error when the data are fitted to the "correct" model (see insets of Fig. 6). Nevertheless, the differences are small and may be hard to disentangle in real biological systems.

In the experiments, the run and tumbling times obtained from the model with speed variability at the population level are both slightly larger than that from the intrinsic-speed-variability model, with an uncertainty of ∼10% which is also slightly larger than that of the intrinsic-speed-variability model (∼5% [31]). We note that in real biological systems, both types of fluctuations are expected; they do not lead to major differences as far as displacement statistics are concerned. We note that implementing the speed variability at the population level allows to work with explicit expression for $f(k, s)$, which, however, have to be inverted numerically.

V. SUMMARY AND CONCLUSION

In this paper, we developed a numerical protocol to quantitatively characterize the tumbling statistics of run-and-tumble bacteria from DDM measurements. First, we showed how to use the renewal theory to calculate the intermediate scattering function of run-and-tumble particles. We proposed two slightly different models, which account for the speed fluctuations at either the intrinsic or the population level. Then we demonstrated a robust protocol to extract parameters from experimental data. The protocol was validated using agent-based simulations and then applied to the experimental data
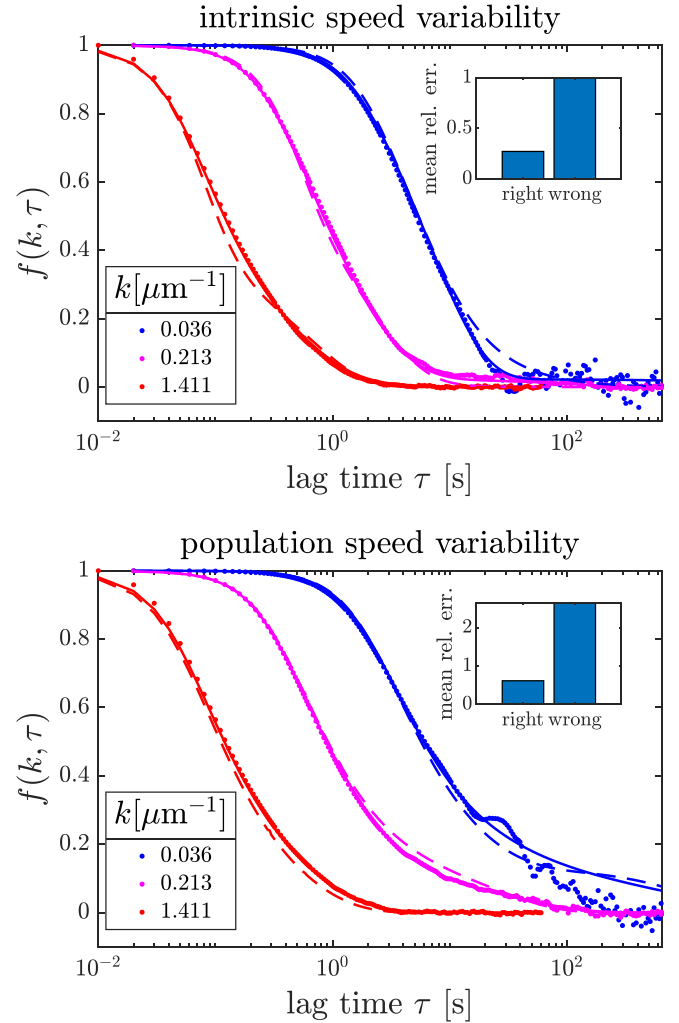
FIG. 6. ISFs obtained from simulations for parameters taken in the regime where the two models are distinguishable. We use the parameters measured for wild-type *E. coli* [31] except for an extremely large σ_v: $\bar{v} = 15.95 \, \mu\text{m s}^{-1}$, $\sigma_v = 15 \, \mu\text{m s}^{-1}$, $D = 0.24 \, \mu\text{m}^2 \, \text{s}^{-1}$, $\alpha = 0.96$, $\tau_R = 2.39$ s, $\tau_T = 0.38$ s. Dots represent simulation data. Solid curves are the fits to the right model, and the dashed curves are fits to the wrong model. We note that the deviation is more significant at small k values. The inset shows the mean relative error $\sum_i |e_i|/6$ of the fitted parameters, where $e_i = (p_{i,\text{fit}} - p_{i,\text{input}})/p_{i,\text{input}}$, and $\mathbf{p} = (\bar{v}, \sigma_v, \tau_R, \tau_T, D, \alpha)$.

of a wild-type *E. coli* AB1157 strain, which was reported in an accompanying paper [31]. At the spatiotemporal scales accessible experimentally, the two models seem to be indistinguishable and the bacteria may in fact exhibit both: intrinsic speed variations and a speed variability at the population level. In [31], we also show how our method can be employed to characterize a transition between perpetual tumbling and smooth swimming in an engineered bacterial strain whose tumbling statistics is under the (now-quantitative) control of a chemical inducer.

The framework of renewal processes is not limited to the RT motion of bacteria and can be extended to other multimode motility patterns, such as the "run-reverse(-flick)" [6–8] or "run-reverse-wrap" [9] motion. In future work, our method

may thus allow for a quantitative characterization of a large variety of microorganisms. Furthermore, the numerical protocol proposed in this paper has vast potential applications, ranging from quantitatively studying the tactic response of individual cells to investigating complex collective bacterial organizations.

In particular, to gain a complete picture of bacterial chemotaxis on the cell level, the regulation of the tumbling statistics due to the presence of spatially varying, external chemical fields [41,42] may be established experimentally by using spatially resolved DDM [39]. The "run-and-tumble" motion has been proposed as a paradigmatic model not only for *E. coli*, but also for many other microorganisms, such as *Euglena gracilis* [43]. The latter can direct its motion in the presence of light sources and its phototaxis has rich features because the cell can sense both the intensity and the polarization of light [44]. Our framework may allow for a quantitative description of this intricate behavior and the associated tumbling statistics.

Finally, the regulation of the tumbling statistics of engineered bacterial strains [31,45] may be exploited for creating complex self-organizations [46,47]. There our high-throughput method could both help validate the design of the engineered strains as well as allow for their quantitative characterization.

APPENDIX A: JACKKNIFE RESAMPLING METHOD

We obtain an estimate of the standard deviation $\text{SE}(\hat{p})$ of the fitted parameters $\hat{p} \in \{\bar{v}, \sigma_v, \tau_R, \tau_T, D, \alpha\}$ using the jackknife resampling method [48]. In our fitting procedure we fit data sets corresponding to N wave numbers $k = \{k_1, \ldots, k_N\}$ simultaneously. The standard jackknife resampling method is based on estimating parameters p_i by omitting the data set corresponding to wave number k_i and thus fitting data sets corresponding to $k = \{k_1, \ldots k_{i-1}, k_{i+1}, \ldots, k_N\}$ only. Repeating this procedure for all wave numbers permits to estimate the jackknife standard deviation as

$$\text{SD}(\hat{p}) = \left[\frac{N-1}{N} \sum_{i=1}^{N} (\bar{p} - p_i)^2 \right]^{1/2}, \quad \text{(A1)}$$

where $\bar{p} = \sum_i p_i / N$ denotes the average over all parameters p_i. The errors of the fitted parameters are then obtained by $\text{SD}(\hat{p})$.

APPENDIX B: AGENT-BASED SIMULATIONS

We have performed agent-based simulations of noninteracting particles in continuous space and time to validate our theoretical predictions and parameter estimation method following previously developed protocols [24,26]. First, we define two types of particles: active agents, which perform run-and-tumble motion, and passive particles, which only diffuse. The active particles alternate between run and tumbling phases. The particles in a run phase move along their swimming direction at constant speed and undergo translational Brownian motion with diffusivity D. The Langevin equation for the ith running particle reads

$$\frac{d\boldsymbol{r}_i}{dt} = v_i \boldsymbol{u}_i + \sqrt{2D} \boldsymbol{\xi}_i, \quad \text{(B1)}$$

where the components $\xi_{i,\alpha}$ are uncorrelated Gaussian white noise such that $\langle \xi_{i,\alpha}(t) \xi_{j,\beta}(t') \rangle = \delta_{ij} \delta_{\alpha\beta} \delta(t - t')$ and $\boldsymbol{u}_i$ is the swimming direction of the ith particle with unit length, $|\boldsymbol{u}_i| = 1$. The swimming speed v_i of the ith particle after each tumbling event is sampled according to the Schultz distribution in Eq. (16). We note that accounting for a speed variability at the population level corresponds to keeping v_i fixed for each cell throughout the simulation, but attributing different v_i to different active particles according to Eq. (16). The tumbling and passive particles perform only translational diffusion with corresponding Langevin equation for the jth tumbling or passive particle, $d\boldsymbol{r}_j / dt = \sqrt{2D} \boldsymbol{\xi}_j$, where D corresponds to the same diffusion coefficient as for running particles. The run time τ_i is distributed according to an exponential distribution with mean run duration τ_R, $\varphi_R(\tau_i) = e^{-\tau_i/\tau_R}/\tau_R$, and the tumbling time τ'_j is distributed according to $\varphi_T(\tau'_j) = e^{-\tau'_j/\tau_T}/\tau_T$, with mean tumbling duration τ_T. The mean run and tumbling durations, τ_R and τ_T, are the same for all particles.

We randomly suspend $N\alpha\tau_R/(\tau_R + \tau_T)$ running particles, $N\alpha\tau_T/(\tau_R + \tau_T)$ tumbling particles, and $(1 - \alpha)N$ passive particles in a cuboid container of size $L \times L \times H$ with periodic boundary conditions. We sample the switching time between run and tumbling phases using a Gillespie stochastic algorithm for all the particles. Then by keeping track of the run and tumbling states of each individual particle, we update the positions of the particles according to the Langevin equations. We generate snapshots at time interval Δt by taking a region $-l/2 < x, y < l/2$, $-h/2 < z < h/2$ in the container, where $l < L$ is the size of the image and $h < H$ is the depth of field, and by selecting all particles suspended in this volume. The snapshot is an image of $N_p \times N_p$ pixels, with pixel size $\delta l = l/N_p$. Then the particle at position (x, y, z) appears in the pixel $(n_x, n_y) = (\lfloor x/\delta l \rfloor, \lfloor y/\delta l \rfloor)$ and its eight neighborhoods, if any of the nine pixels are in the range $[0, N_p - 1] \times [0, N_p - 1]$. Denoting $\delta x = x/\delta l - n_x$, $\delta x' = \min\{\delta x, 1 - \delta x\}$, $\delta y = y/\delta l - n_y$, and $\delta y' = \min\{\delta y, 1 - \delta y\}$, the intensity of a single particle is spread out over the nine adjacent pixels as

$$I_{n_x+m, n_y+l} = C(z) I_m(\delta x) I_l(\delta y), \quad \text{(B2)}$$

where $m, l = 0, \pm 1$, $C(z) = 1 - 4z^2/h^2$ is the contrast function, and

$$I_m(\delta x) = \frac{\delta_{m,-1}(1 - \delta x) + \delta_{m,0}(1 + \delta x') + \delta_{m,1}\delta x}{2 + \delta x'},$$

$$\text{(B3a)}$$

$$I_l(\delta y) = \frac{\delta_{l,-1}(1 - \delta y) + \delta_{l,0}(1 + \delta y') + \delta_{l,1}\delta y}{2 + \delta y'}. \quad \text{(B3b)}$$

Finally, we sum the image intensities corresponding to all the particles to generate a snapshot [see Fig. 3(a) for an example]. Similarly to the experimental setup described in Ref. [31], we generate snapshots from data measured at two different magnifications. In particular, we sample low-magnification data with pixel size $\delta\ell = 6.5$ μm, time step $\Delta t = 0.02$ s over a total time of 640 s, and depth of field $h = 400$ μm using a simulation box of size 4000 μm$\times$4000 μm$\times$

500 μm. The small-length-scale data are measured at a higher magnification: The corresponding parameters are $\delta\ell = 1.4$ μm, $\Delta t = 0.01$ s over a total time of 65 s, and $h = 80$ μm using a simulation box of size 1000 μm$\times$1000 μm$\times$160 μm. In both cases the number of pixels is $N_p \times N_p = 512 \times 512$. To mimic the experimental procedure, we then apply the DDM analysis described in Sec. III A to extract the ISFs from the generated simulation snapshots.

[1] P. Romanczuk, M. Bär, W. Ebeling, B. Lindner, and L. Schimansky-Geier, Active Brownian particles, Eur. Phys. J. Spec. Top. **202**, 1 (2012).

[2] J. Elgeti, R. G. Winkler, and G. Gompper, Physics of microswimmers—Single particle motion and collective behavior: A review, Rep. Prog. Phys. **78**, 056601 (2015).

[3] C. Bechinger, R. Di Leonardo, H. Löwen, C. Reichhardt, G. Volpe, and G. Volpe, Active particles in complex and crowded environments, Rev. Mod. Phys. **88**, 045006 (2016).

[4] O. Bénichou, C. Loverdo, M. Moreau, and R. Voituriez, Intermittent search strategies, Rev. Mod. Phys. **83**, 81 (2011).

[5] G. H. Wadhams and J. P. Armitage, Making sense of it all: Bacterial chemotaxis, Nat. Rev. Mol. Cell Biol. **5**, 1024 (2004).

[6] J. Taktikos, H. Stark, and V. Zaburdaev, How the motility pattern of bacteria affects their dispersal and chemotaxis, PLoS ONE **8**, e81936 (2013).

[7] K. Taute, S. Gude, S. Tans, and T. Shimizu, High-throughput 3D tracking of bacteria on a standard phase contrast microscope, Nat. Commun. **6**, 8776 (2015).

[8] K. L. Thornton, J. K. Butler, S. J. Davis, B. K. Baxter, and L. G. Wilson, Haloarchaea swim slowly for optimal chemotactic efficiency in low nutrient environments, Nat. Commun. **11**, 1 (2020).

[9] Z. Alirezaeizanjani, R. Großmann, V. Pfeifer, M. Hintsche, and C. Beta, Chemotaxis strategies of bacteria with multiple run modes, Sci. Adv. **6**, eaaz6153 (2020).

[10] M. Polin, I. Tuval, K. Drescher, J. P. Gollub, and R. E. Goldstein, Chlamydomonas swims with two "gears" in a eukaryotic version of run-and-tumble locomotion, Science **325**, 487 (2009).

[11] H. C. Berg and D. A. Brown, Chemotaxis in *Escherichia coli* analysed by three-dimensional tracking, Nature (London) **239**, 500 (1972).

[12] M. J. Schnitzer, Theory of continuum random walks and application to chemotaxis, Phys. Rev. E **48**, 2553 (1993).

[13] A. Celani and M. Vergassola, Bacterial strategies for chemotaxis response, Proc. Natl. Acad. Sci. USA **107**, 1391 (2010).

[14] S. Chatterjee, R. A. da Silveira, and Y. Kafri, Chemotaxis when bacteria remember: Drift versus diffusion, PLoS Comput. Biol. **7**, e1002283 (2011).

[15] J. Saragosti, P. Silberzan, and A. Buguin, Modeling *E. coli* tumbles by rotational diffusion. Implications for chemotaxis, PLoS ONE **7**, e35412 (2012).

[16] P. S. Lovely and F. Dahlquist, Statistical measures of bacterial motility and chemotaxis, J. Theor. Biol. **50**, 477 (1975).

[17] M. E. Cates and J. Tailleur, When are active Brownian particles and run-and-tumble particles equivalent? Consequences for motility-induced phase separation, Europhys. Lett. **101**, 20010 (2013).

[18] E. Lauga, W. R. DiLuzio, G. M. Whitesides, and H. A. Stone, Swimming in circles: Motion of bacteria near solid boundaries, Biophys. J. **90**, 400 (2006).

[19] R. Di Leonardo, D. Dell'Arciprete, L. Angelani, and V. Iebba, Swimming with an image, Phys. Rev. Lett. **106**, 038101 (2011).

[20] G. Junot, T. Darnige, A. Lindner, V. A. Martinez, J. Arlt, A. Dawson, W. C. K. Poon, H. Auradou, and E. Clément, Run-to-tumble variability controls the surface residence times of *E. coli* bacteria, Phys. Rev. Lett. **128**, 248101 (2022).

[21] P. Cluzel, M. Surette, and S. Leibler, An ultrasensitive bacterial motor revealed by monitoring signaling proteins in single cells, Science **287**, 1652 (2000).

[22] E. Korobkova, T. Emonet, J. M. Vilar, T. S. Shimizu, and P. Cluzel, From molecular noise to behavioural variability in a single bacterium, Nature (London) **428**, 574 (2004).

[23] R. Cerbino and V. Trappe, Differential dynamic microscopy: Probing wave vector dependent dynamics with a microscope, Phys. Rev. Lett. **100**, 188102 (2008).

[24] L. G. Wilson, V. A. Martinez, J. Schwarz-Linek, J. Tailleur, G. Bryant, P. N. Pusey, and W. C. K. Poon, Differential dynamic microscopy of bacterial motility, Phys. Rev. Lett. **106**, 018101 (2011).

[25] C. Kurzthaler, C. Devailly, J. Arlt, T. Franosch, W. C. K. Poon, V. A. Martinez, and A. T. Brown, Probing the spatiotemporal dynamics of catalytic Janus particles with single-particle tracking and differential dynamic microscopy, Phys. Rev. Lett. **121**, 078001 (2018).

[26] V. A. Martinez, R. Besseling, O. A. Croze, J. Tailleur, M. Reufer, J. Schwarz-Linek, L. G. Wilson, M. A. Bees, and W. C. K. Poon, Differential dynamic microscopy: A high-throughput method for characterizing the motility of microorganisms, Biophys. J. **103**, 1637 (2012).

[27] A. Jepson, J. Arlt, J. Statham, M. Spilman, K. Burton, T. Wood, W. C. Poon, and V. A. Martinez, High-throughput characterisation of bull semen motility using differential dynamic microscopy, PLoS ONE **14**, e0202720 (2019).

[28] O. A. Croze, V. A. Martinez, T. Jakuszeit, D. Dell'Arciprete, W. C. Poon, and M. A. Bees, Helical and oscillatory microswimmer motility statistics from differential dynamic microscopy, New J. Phys. **21**, 063012 (2019).

[29] L. Angelani, Averaged run-and-tumble walks, Europhys. Lett. **102**, 20004 (2013).

[30] K. Martens, L. Angelani, R. Di Leonardo, and L. Bocquet, Probability distributions for the run-and-tumble bacterial

dynamics: An analogy to the Lorentz model, Eur. Phys. J. E **35**, 84 (2012).

[31] C. Kurzthaler, Y. Zhao, N. Zhou, J. Schwarz-Linek, C. Devailly, J. Arlt, J. D. Huang, W. C. K. Poon, T. Franosch, J. Tailleur, and V. A. Martinez, companion paper, Characterization and control of the run-and-tumble dynamics of *Escherichia coli*, Phys. Rev. Lett. **132**, 038302 (2024).

[32] W. Feller, *An Introduction to Probability Theory and Its Applications*, Vol. II (John Wiley & Sons, New York, 1971).

[33] V. Méndez, D. Campos, and F. Bartumeus, *Stochastic Foundations in Movement Ecology* (Springer-Verlag, Berlin, 2014).

[34] V. Zaburdaev, S. Denisov, and J. Klafter, Lévy walks, Rev. Mod. Phys. **87**, 483 (2015).

[35] F. Detcheverry, Unimodal and bimodal random motions of independent exponential steps, Eur. Phys. J. E **37**, 114 (2014).

[36] L. Turner, L. Ping, M. Neubauer, and H. C. Berg, Visualizing flagella while tracking bacteria, Biophys. J. **111**, 630 (2016).

[37] W. T. Weeks, Numerical inversion of Laplace transforms using Laguerre functions, J. ACM **13**, 419 (1966).

[38] J. A. C. Weideman, Algorithms for parameter selection in the weeks method for inverting the Laplace transform, SIAM J. Sci. Comput. **21**, 111 (1999).

[39] M. Reufer, V. A. Martinez, P. Schurtenberger, and W. C. K. Poon, Differential dynamic microscopy for anisotropic colloidal dynamics, Langmuir **28**, 4618 (2012).

[40] J. A. Nelder and R. Mead, A simplex method for function minimization, Comput. J. **7**, 308 (1965).

[41] D. A. Clark and L. C. Grant, The bacterial chemotactic response reflects a compromise between transient and steady-state behavior, Proc. Natl. Acad. Sci. USA **102**, 9150 (2005).

[42] Y. Kafri and R. A. da Silveira, Steady-state chemotaxis in *Escherichia coli*, Phys. Rev. Lett. **100**, 238101 (2008).

[43] A. C. Tsang, A. T. Lam, and I. H. Riedel-Kruse, Polygonal motion and adaptable phototaxis via flagellar beat switching in the microswimmer *Euglena gracilis*, Nat. Phys. **14**, 1216 (2018).

[44] S. Yang, M. Huang, Y. Zhao, and H. P. Zhang, Controlling cell motion and microscale flow with polarized light fields, Phys. Rev. Lett. **126**, 058001 (2021).

[45] R. McKay, P. Hauk, H.-C. Wu, A. E. Pottash, W. Shang, J. Terrell, G. F. Payne, and W. E. Bentley, Controlling localization of escherichia coli populations using a two-part synthetic motility circuit: An accelerator and brake, Biotechnol. Bioeng. **114**, 2883 (2017).

[46] C. Liu, X. Fu, L. Liu, X. Ren, C. K. Chau, S. Li, L. Xiang, H. Zeng, G. Chen, L.-H. Tang *et al.*, Sequential establishment of stripe patterns in an expanding cell population, Science **334**, 238 (2011).

[47] A. Curatolo, N. Zhou, Y. Zhao, C. Liu, A. Daerr, J. Tailleur, and J. Huang, Cooperative pattern formation in multi-component bacterial systems through reciprocal motility regulation, Nat. Phys. **16**, 1152 (2020).

[48] B. Efron, Nonparametric estimates of standard error: The jackknife, the bootstrap and other methods, Biometrika **68**, 589 (1981).